Itinerant ferromagnetism of the Pd-terminated polar surface of $PdCoO_2$

Federico Mazzola[a], Veronika Sunko[a,b], Seunghyun Khim[b], Helge Rosner[b], Pallavi Kushwaha[b], Oliver J. Clark[a], Lewis Bawden[a], Igor Marković[a,b], Timur K. Kim[c], Moritz Hoesch[c], Andrew P. Mackenzie[b,a,1], and Phil D. C. King[a,1]

[a]Scottish Universities Physics Alliance, School of Physics and Astronomy, University of St. Andrews, St. Andrews KY16 9SS, United Kingdom; [b]Max Planck Institute for Chemical Physics of Solids, 01187 Dresden, Germany; and [c]Diamond Light Source, Didcot, OX11 0DE, United Kingdom

Edited by Zachary Fisk, University of California, Irvine, CA, and approved November 5, 2018 (received for review July 10, 2018)

The ability to modulate the collective properties of correlated electron systems at their interfaces and surfaces underpins the burgeoning field of "designer" quantum materials. Here, we show how an electronic reconstruction driven by surface polarity mediates a Stoner-like magnetic instability to itinerant ferromagnetism at the Pd-terminated surface of the nonmagnetic delafossite oxide metal $PdCoO_2$. Combining angle-resolved photoemission spectroscopy and density-functional theory calculations, we show how this leads to a rich multiband surface electronic structure. We find similar surface state dispersions in $PdCrO_2$, suggesting surface ferromagnetism persists in this sister compound despite its bulk antiferromagnetic order.

delafossite | itinerant ferromagnetism | electronic reconstruction | transition-metal oxide | angle-resolved photoemission

Recent advances in the ability to fabricate transition-metal oxides with atomic-scale precision provide interesting opportunities for controlling their quantum many-body states and phases (1–10). A prototypical example is the interface between the bulk insulating perovskite oxides $SrTiO_3$ and $LaAlO_3$, which supports a 2D electron liquid (11) hosting a number of remarkable properties, from gate-tuneable superconductivity (12) to magnetic order (13). The emergence of conductivity in this system is thought to be intricately linked to the polar nature of the interface between $SrTiO_3$ and $LaAlO_3$ (11, 14, 15). The carrier densities observed, however, are typically an order of magnitude smaller than would be expected from a pure electronic reconstruction driven by the so-called polar catastrophe (12, 15, 16), and the microscopic mechanism by which polarity may mediate a conducting interface has proved controversial (17–22). It is important, therefore, to investigate the influence of surface and interface polarity in other transition metal-based oxides, both for developing improved understanding and for expanding the search of materials systems that may host novel surface or interface phases.

Here, we focus on the "ABO_2" delafossite oxides (23–28). Delafossites represent a particularly promising material class both because of their naturally layered structure and the potential to drastically alter their physical properties by changing the A- and B-site cations (29–31). Bulk $MCoO_2$ (M = Pt,Pd) are nonmagnetic metals with simple single-band Fermi surfaces. They exhibit the highest conductivity of all known metallic oxides (26, 28, 32–34). They also host polar surfaces, opening the potential to stabilize local electronic environments and phases different to those of the bulk (35–37). We use angle-resolved photoemission spectroscopy (ARPES) to probe the Pd-terminated surface electronic structure of $PdCoO_2$. In agreement with our calculations from density-functional theory (DFT), these experiments demonstrate how the polarity induces a pronounced electron doping at the surface, which in turn mediates an intrinsic Stoner instability toward itinerant ferromagnetism. We find that a similar surface ferromagnetism persists in the sister compound $PdCrO_2$, which is antiferromagnetically ordered in the bulk. This points to an exciting opportunity to use polar surfaces and interfaces to induce new magnetic states in oxides as well as to generate naturally occurring magnetic heterostructures.

Results

Surface Termination-Dependent Measurements. $PdCoO_2$ is comprised of triangular-lattice metallic Pd planes separated by insulating CoO_2 layers. This crystal structure has natural cleavage planes above and below each Pd layer: Inequivalent surface terminations would therefore be expected (Fig. 1*A*). Consistent with this, we find a strong variation in the relative intensity of Co $3p$ and Pd $4p$ core levels measured by X-ray photoelectron spectroscopy (XPS) at different patches of the cleaved sample surface (Fig. 1*B*). This is correlated with a marked difference in the electronic structure measured by ARPES (Fig. 1 *C*–*E*). Across the sample, we find a steeply dispersive state that we attribute as the Pd-derived bulk band (36). In Fig. 1*C*, our measurements additionally show a pair of massive hole-like bands (Fig. 1*C*, labeled "S-CoO_2"). These have been assigned previously as surface states from the CoO_2 termination (36, 37), consistent with our XPS measurements from the same sample region, which yield the greatest ratio of Co $3p$:Pd $4p$ core-level spectral weight.

Measurements from a different patch of the same sample (Fig. 1*E*) reveal a completely different surface electronic

Significance

There has been widespread interest in using interfaces of transition-metal oxides as a platform to control not only their electronic structure, as in semiconductor heterostructures, but also to tune between different collective phases. A major goal is to realize states of the quantum many-body system that are not found in the bulk phase diagrams of the constituent materials. Here, we perform a combined experimental and theoretical study of the delafossite oxide metals $PdCoO_2$ and $PdCrO_2$, finding how electronic reconstructions at their polar surfaces drive instabilities to itinerant surface ferromagnetism. Neither compound supports ferromagnetism in bulk, with $PdCrO_2$ a bulk antiferromagnet, demonstrating how a delicate competition of magnetic correlations can be engineered by intrinsic self-doping at a polar surface or interface.

Author contributions: F.M., V.S., A.P.M., and P.D.C.K. designed research; F.M., V.S., S.K., H.R., P.K., O.J.C., L.B., I.M., T.K.K., M.H., and P.D.C.K. performed research; F.M. analyzed data; and F.M., V.S., A.P.M., and P.D.C.K. wrote the paper.

The authors declare no conflict of interest.

This article is a PNAS Direct Submission.

Data deposition: The data that underpins the findings of this study are available from the University of St Andrews research portal, https://doi.org/10.17630/fcc2f304-6bec-4fd9-94d2-02ee8fff065f.

[1]To whom correspondence may be addressed. Email: philip.king@st-andrews.ac.uk or andy.mackenzie@cpfs.mpg.de.

This article contains supporting information online at www.pnas.org/lookup/suppl/doi:10.1073/pnas.1811873115/-/DCSupplemental.

Published online December 4, 2018.

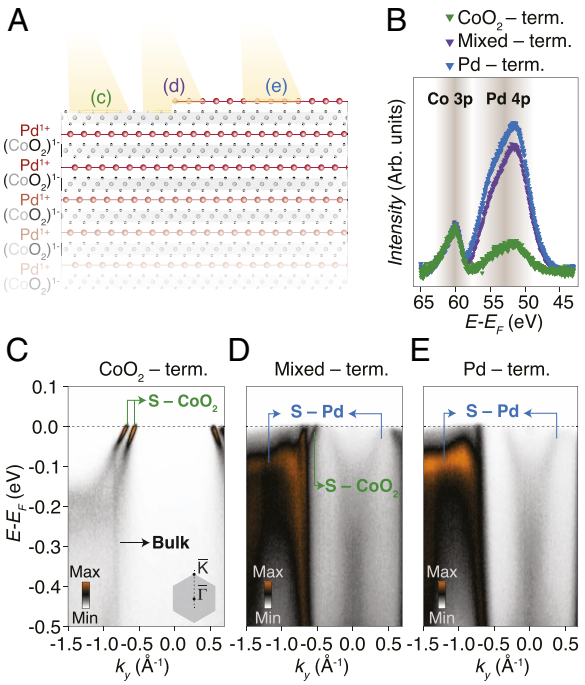

Fig. 1. Surface terminations of $PdCoO_2$. (*A*) Side view of the crystal structure of $PdCoO_2$, showing two possible surface terminations that can be expected. (*B*) XPS spectra ($h\nu = 120$ eV, after subtraction of a linear background and normalized by the area of the Co 3p peak) at different spatial locations of a cleaved crystal show varying relative ratios of Co and Pd core level peaks, consistent with a spatial dependence of the dominant surface termination. (*C*–*E*) Markedly different electronic structures are observed by ARPES ($h\nu = 90$ eV, *p*-polarization, measured along $\bar{\Gamma} - \bar{K}$) at these locations, corresponding to predominantly (*C*) CoO_2, (*E*) Pd, and (*D*) mixed-surface terminations.

structure, which we describe in detail below. Our XPS measurements exhibit a much larger spectral weight of the Pd than the Co-derived core-level peak for this sample region (Fig. 1*B*), and we thus attribute these as surface states originating from the Pd-terminated surface ("S-Pd"). We note that for most regions where such states are visible, we observe a superposition of these spectral features with those of the CoO_2-terminated surface (e.g., Fig. 1*D*). This indicates a rather limited spatial extent of typical Pd-terminated regions, with a mixed surface termination within our probing light spot area ($\sim$50 μm diameter). In the following, we show our highest quality ARPES data obtained from a sample that exhibits such a mixed surface terminations. Similar results were obtained from multiple samples.

Pd-Terminated Surface Electronic Structure. The measured Fermi surfaces and dispersions from such a mixed surface termination are shown in Fig. 2. The CoO_2-terminated surface states form hexagonal and nearly circular hole-like Fermi surfaces about the Brillouin zone center, split-off by a surprisingly large Rashba-like interaction arising due to a large energy scale of inversion symmetry breaking at this surface (37). We do not consider these further here.

Two larger electron-like Fermi surfaces with sharp linewidths are also visible. From comparison with previous experiments (32, 36), we attribute the largest of these as the Pd-derived bulk Fermi surface. The other has a similar topography but slightly smaller average k_F and has greater spectral weight when measured in the second Brillouin zone (Fig. 2*A*). This band is also evident as a steeply dispersing state in our measured dispersions (Fig. 2*B*) and appears to be an approximate replica of the bulk state but shifted toward the Fermi level by $\sim$430 meV. In principle, it is not surprising for a polar charge to change the binding energy of states localized at a polar surface. Indeed, for the CoO_2-terminated surface, the absence of Pd atoms above the topmost CoO_2 block leads to a formal valence of 3.5+ rather than 3+ for the surface Co layer, corresponding to an experimentally observed (35, 37) effective hole-doping of $\approx$0.5 holes per unit cell. Similar electrostatic arguments for the Pd-terminated surface (35) would suggest a formal valence of $Pd^{0.5+}$ at the surface, compared with Pd^{1+} in the bulk. This, however, should manifest as a surface doping of $\approx$0.5 electrons per unit cell, seemingly in contrast to the hole-doped copy of the bulk band observed experimentally here.

Moreover, rather than a simple rigid shift of the bulk Pd-derived valence band, our measured dispersions (Fig. 2 *B* and *C*)

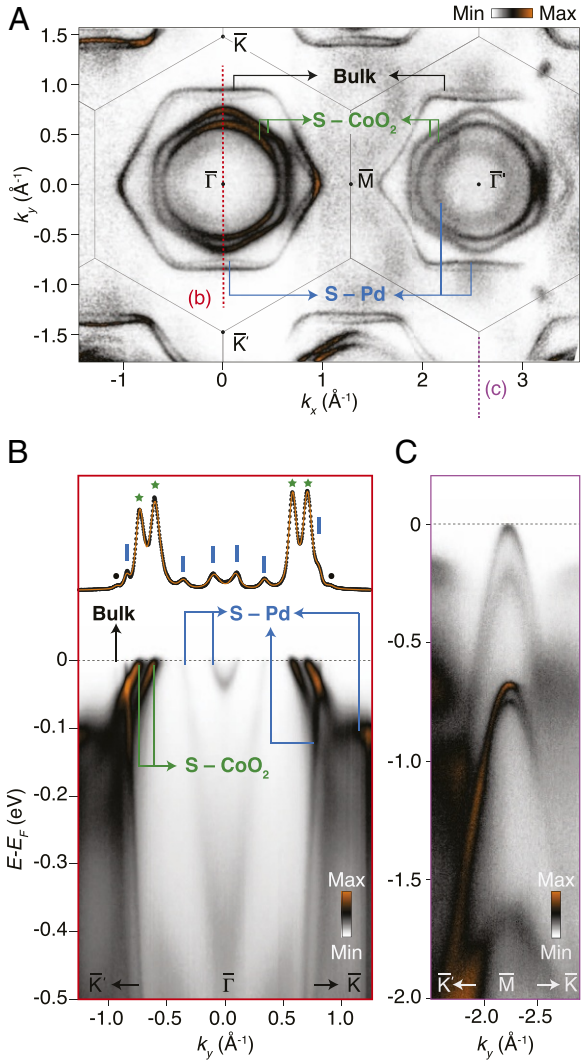

Fig. 2. Surface electronic structure. (*A*) ARPES Fermi surface ($h\nu = 110$ eV, $E_F \pm 15$ meV, *p*-pol.) and dispersions ($h\nu = 80$ eV, *p*-pol.) measured along (*B*) $\bar{\Gamma} - \bar{K}$ and (*C*) $\bar{M} - \bar{K}$. As well as the bulk band (Bulk), a series of additional surface states arising from the Pd-terminated (S-Pd) and CoO_2-terminated (S-CoO_2) surfaces are visible. A momentum distribution curve (MDC) at the Fermi level ($E_F \pm 5$ meV) is shown in *B*, together with a 12-band peak fit (orange line) and corresponding Fermi momenta (marked by dashes, stars, and dots, for S-Pd, S-CoO_2, and bulk, respectively) of such bulk and surface states that cross E_F.

reveal a much richer surface electronic structure. As well as the steep band discussed above, Fig. 2*B* shows a flat-topped band located ∼100 meV below the Fermi level and a pair of electron-like bands crossing E_F near the Brillouin zone center (all labeled S-Pd in Fig. 2*B*). The outer of these electron pockets can also be seen in our Fermi surface measurements (Fig. 2*A*), while the innermost band is not clearly observed at the photon energy used. Additionally, multiple fully occupied bands are found at the Brillouin zone face $\overline{\mathrm{M}}$-point (Fig. 2*C*).

Itinerant Surface Ferromagnetism. We demonstrate below that such a rich multiband electronic structure of the Pd-terminated surface of $PdCoO_2$ is the result of an instability to itinerant surface ferromagnetism. Fig. 3 shows the dispersions of the bulk and Pd-derived surface states extracted from the measurements shown in Fig. 2*B* as well as from equivalent measurements performed using a different photon energy and/or light polarization. These different experimental conditions lead to varying transition matrix elements, selectively enhancing the visibility of different features (see, for example, *SI Appendix*, Fig. S1), thus ensuring that we capture the dispersions of all bands accurately. If we assume that these surface states are spin-degenerate and extract their Luttinger count from our experimentally measured Fermi surfaces, we find an electron count that is unphysically high. In contrast, if we treat them as spin-polarized, we find a surface carrier density that is 0.55 ± 0.03 electrons per unit cell higher than that of the bulk, which is close to the additional 0.5 electrons per unit cell that would be expected from the polar surface charge. We note that spin-polarized states are generically allowed at surfaces, where the breaking of inversion symmetry can lead to a momentum-dependent spin-splitting of the Rashba-type (38). If this was the origin of the surface state spin polarization here, however, then the spin-splitting should vanish at the zero-momentum $\overline{\Gamma}$-point, where time-reversal symmetry enforces a Kramers degeneracy. In contrast, the clear splitting of spin-polarized bands that we observe at the $\overline{\Gamma}$ point (Figs. 2*B* and 3) indicates that time-reversal symmetry is broken here [i.e., $E(k=0,\uparrow) \neq E(k=0,\downarrow)$]. Moreover, a Rashba-like origin of the observed spin-polarized bands would be incompatible with the large (≈430 meV) energy splitting of the steep bands that we observe, which is more than three times the atomic

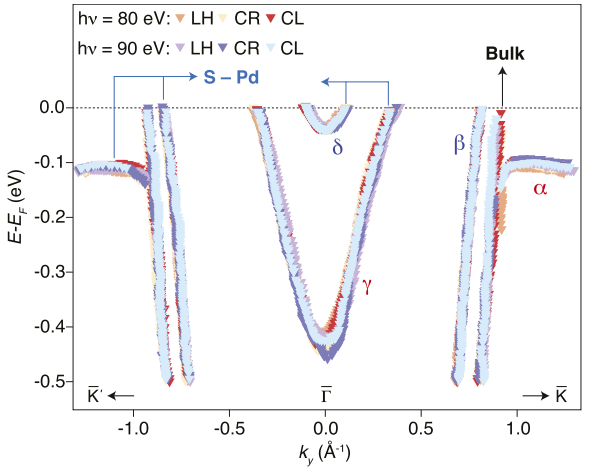

Fig. 3. Itinerant surface ferromagnetism in $PdCoO_2$. Bulk and surface band dispersions exacted from ARPES measurements using different photon energies and light polarizations: linear horizontal (LH, *p*-polarization), circular right (CR), and circular left (CL) polarizations.

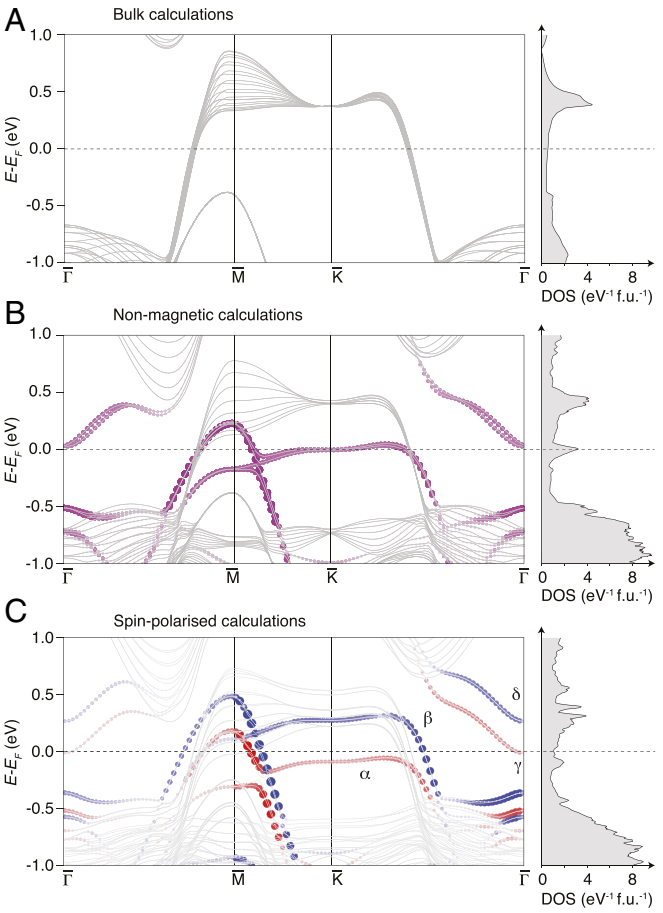

Fig. 4. DFT supercell calculations and electron DOS. (*A*) Bulk k_z-projected electronic structure of $PdCoO_2$ (*Left*) and corresponding electron DOS (*Right*). (*B*) Nonmagnetic supercell calculations (*Left*), showing the formation of a flat surface state right at the Fermi level, leading to a large peak in the corresponding density of states (DOS) (*Right*). Additionally, a moderate Rasbha-like spin-orbit splitting of the electron band near the $\overline{\Gamma}$-point is observed. The calculations are projected onto the surface Pd layer (purple coloring) to highlight the surface states. (*C*) Spin-polarized supercell calculations (*Left*) indicate how a Stoner-like transition spin-splits the states, giving rise to the $\alpha - \beta$ and $\gamma - \delta$ exchange-split pairs discussed in the main text. The spin majority and minority character as projected onto the surface Pd layer is shown by red and blue coloring, respectively.

spin-orbit coupling of Pd.* Together, these observations therefore rule out a Rashba origin of our observed spin-polarized surface states; instead, they provide conclusive empirical evidence that the Pd-terminated surface of $PdCoO_2$ is ferromagnetic.

Although the above conclusion is independent of theory, it is also reinforced by explicit calculations (Fig. 4; see *Materials and Methods*), which further demonstrate how the surface ferromagnetism arises as a result of an intrinsic Stoner-like instability driven by the polar surface charge. This mechanism is shown in Fig. 4. The band that forms the bulk Fermi surface, while steep at the Fermi level (34, 39), becomes much flatter above

*We note that our nonmagnetic calculations (Fig. 4*B*) show a Rashba-like spin splitting on the order of 50 meV, a realistic value given the atomic spin-orbit strength of ≈110 meV. This is, however, significantly smaller than the exchange splitting observed experimentally as well as that found from our spin-polarized calculations. We thus conclude that Rashba-type interactions do not play a significant role here compared with magnetic correlations. Whether they play a role in determining the detailed magnetic structure, for example in stabilizing noncollinear magnetic states, is an interesting question for future study.

E_F (evident, for example, along $\bar{\Gamma}-\bar{K}$ in the bulk k_z-projected calculations shown in Fig. 4*A*). Compensating the surface polarity should lead to electron doping of the surface layer, as discussed above. This will create a surface copy of the bulk band. Its flat band top and the high DOS associated with it are pushed downward toward the Fermi level, as evident in our nonmagnetic supercell calculations shown in Fig. 4*B*. From a spin-polarized calculation (Fig. 4*C*), we find that the DOS at E_F is sufficiently high to trigger a Stoner transition. The band at the Fermi level therefore exchange splits into a pair of spin-polarized bands (labeled α and β), which can be identified as the experimentally observed flat (α in Fig. 3) and steep (β) states. Consistent with previous DFT calculations (35), we also find how additional near-E_F surface states inherit a similar exchange splitting, forming the majority-spin and minority-spin γ and δ bands observed at the Brillouin zone center in our ARPES measurements (Fig. 3).

We note that the surface magnetism observed here is thus qualitatively different to the recent observations of ferromagnetism arising due to uncompensated moments at the surface of, for example, antiferromagnetic (AF) $EuRh_2Si_2$ (40). Instead, it reflects an intrinsic instability of the underlying electronic structure that can be triggered by a pronounced self-doping of the system in response to its polar surface charge. From our extracted Luttinger areas, we estimate a total magnetization, $M=(N^{\uparrow}-N^{\downarrow})\mu_B=(0.59\pm0.03)\mu_B$ per unit cell. As the wavefunctions of the surface states are mostly localized on the surface Pd layer (see *SI Appendix*, Fig. S2), this layer also hosts the largest moment (found to be 0.46 μ_B in our calculations; see *Materials and Methods*). Nonetheless, finite orbital mixing with the subsurface CoO_2 block means that the near-surface Co also inherits a finite, but much smaller, moment, found to be 0.12 μ_B in our calculations.

Ferromagnetic Surface of $PdCrO_2$. Finally, we show our measurements of the Pd-terminated surface of the sister compound, $PdCrO_2$ (Fig. 5). As in $PdCoO_2$, the bulk band, which is also responsible for the high bulk conductivity of $PdCrO_2$ (41), is evident as a steeply dispersing state with the largest k_F. We again observe a copy of this state shifted toward the Fermi level (labeled "β" in analogy with the $PdCoO_2$ case discussed above), an α-band with its flat top at $\approx$150 meV below the Fermi level and, in this case, a single electron-like (γ) band crossing E_F near the Brillouin zone center. This electronic structure is consistent with previous measurements of the chromate (42). Moreover, there is an almost one-to-one correspondence with the surface states that we observe for the Pd-terminated surface of $PdCoO_2$, allowing us to again assign the α and β bands as an exchange-split pair in $PdCrO_2$, and the γ-band as a spin-majority band, with its spin-minority partner being unoccupied. Excitingly, while the CoO_2 layer in $PdCoO_2$ is band insulating and nonmagnetic, the CrO_2 layer in bulk $PdCrO_2$ is Mott insulating and hosts local-moment AF order on the Cr sites (41). Combined with the analysis of $PdCoO_2$ presented above, however, our measurements indicate that $PdCrO_2$ nonetheless also supports ferromagnetism at its Pd-terminated surface.

Discussion

Together, our findings demonstrate how electronic reconstructions at polar surfaces can be exploited to trigger incipient instabilities of the underlying quantum many-body system, here driving a Stoner transition at the Pd-terminated surfaces of $PdCoO_2$ and $PdCrO_2$. This suggests strategies for creating 2D ferromagnets, a topic that has been attracting considerable recent attention in the field of van der Waals materials (43, 44). The coexistence of ferromagnetism with the inherent breaking of inversion symmetry at the surface further opens possibilities to realize significant Dzyaloshinskii–Moriya interactions, providing routes to stabilize modulated magnetic states (45).

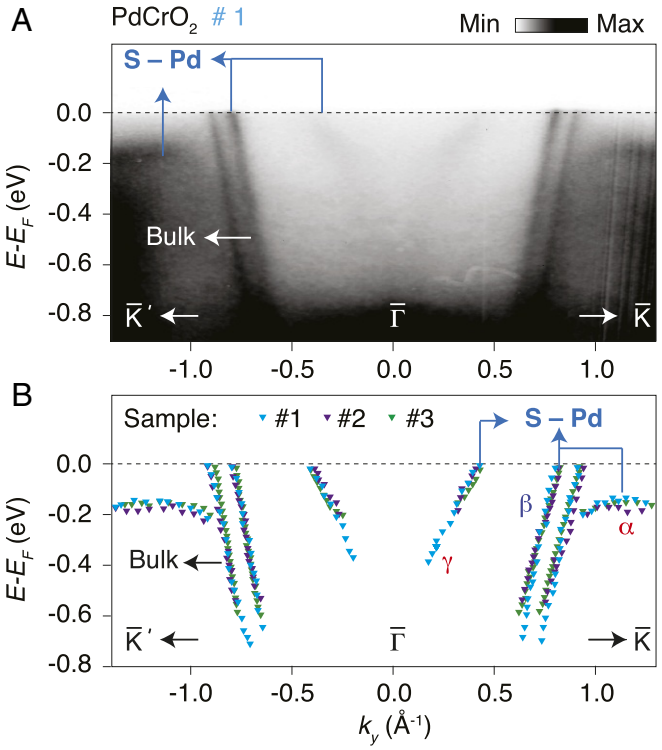

Fig. 5. Itinerant surface ferromagnetism in $PdCrO_2$. (*A*) ARPES spectra of $PdCrO_2$, measured along the $\bar{\Gamma}-\bar{K}$ direction ($h\nu=90$ eV, *p*-pol.). (*B*) Corresponding band dispersions extracted from the data shown in *A* (blue color) as well as additional band dispersions from other samples (#2, $h\nu=100$ eV, *p*-pol. and #3, $h\nu=110$ eV, *p*-pol.). The flat α and steep β exchange-split pair evident in $PdCoO_2$ (Fig. 3*A*) are also observed here as well as the electron-pocket of the spin-majority γ band. The spin-minority δ band appears to be fully unoccupied.

Moreover, creating interfaces between disparate magnetic systems offers powerful opportunities for tailoring magnetic interactions (46). This is of both fundamental interest and potential technological applicability, for example enabling the electrical switching of magnetization in ferromagnetic/AF bilayers (47). Our study indicates how such magnetic heterostructures can naturally be realized at the Pd-terminated surface of $PdCrO_2$. Targeted engineering of magnetic competition could be further aided by the flexibility of the delafossite oxide series. For example, electron doping on the Pd site of $PdCrO_2$ could be used to drive a Stoner transition of the bulk Pd layers, forming an intrinsic superlattice of 2D itinerant ferromagnets and triangular-lattice local-moment AFs. Polar interfaces of delafossites with other materials provide further routes to create and manipulate rich electronic and magnetic phase diagrams in these systems. More generally, our study further highlights the powerful role that polar interfaces can be expected to play not only in controlling electronic structures but also for determining the collective phases that can be stabilized, opening routes for the targeted creation and manipulation of multifunctional designer oxide heterostructures.

Materials and Methods

Angle-Resolved-Photoemission. Single crystals of $PdCoO_2$ and $PdCrO_2$ were grown by a flux method in sealed quartz tubes (26, 48). These were cleaved in situ at the measurement temperature of $T\sim10$ K. ARPES measurements were performed at the I05 beamline of Diamond Light Source using a Scienta R4000 electron analyzer and variable light polarizations with photon energies between 60 and 120 eV (49).

DFT. DFT calculations were performed using the full-potential local-orbital (FPLO) code (www.fplo.de, version fplo14.00-47) (50–52), using the Perdew–Burke–Ernzerhof (52) formalism and including spin–orbit coupling. The surface electronic structure was calculated using a symmetric slab containing 9 Pd layers, with a vacuum gap of 15 Å. For the inner layers of the slab, the bulk experimental crystal structure (34) was used, while the surface atomic positions were relaxed. We note that, for the unrelaxed surface, we do not stabilize a magnetic state. By fully relaxing the topmost Pd layer to minimize forces on the surface Pd atoms, we obtain a sizable increase of the Pd–O distance and find a stable ferromagnetic state with a magnetic moment of 0.55 μ_B per unit cell. The moment is predominantly carried by the surface Pd (0.40 μ_B) with minor contributions from the subsurface Co (0.10 μ_B) and O (0.04 μ_B) just below the surface. As shown in *SI Appendix*, Fig. S3, the peak at the Fermi level deriving from the Pd-related surface state becomes considerably narrower for the relaxed surface with the increased Pd–O distance compared with the unrelaxed one. This leads to a strong increase (by about 50%) of the DOS (E_F) and the respective Pd 4*d* DOS, strongly favoring a magnetic splitting of these states in a Stoner picture. The stability of the ferromagnetic surface state slightly increases if not only the surface Pd but also the CoO_2 layer nearest the surface is relaxed, increasing the magnetic moment to 0.62 μ_B per unit cell (Pd: 0.46 μ_B; Co: 0.12 μ_B; O: 0.05 μ_B). These structural relaxations are used for the calculations presented in the main text. For the DOS shown in Fig. 4, a boxcar smoothing of 25 meV has been used to remove unphysical spikes appearing in the calculated DOS for the supercell.

Experimentally, we find that the surface states at $\overline{M}$ are all located below E_F (Fig. 2*C*), unlike for our supercell calculations. In general, we note that the exact ordering of bulk and different surface features in our calculations is sensitive to application of a Hubbard U term on the Co sites as well as an intrinsic off-stoichiometry of the slab due to the polar nature of the structure. Taking into account the strong Coulomb repulsion at the Co-site in a mean field way, applying DFT + U [U = 4 eV (37)], the total moment remains almost unchanged, but the contribution of Pd increases sizeably (Pd: 0.54 μ_B; Co: 0.05 μ_B; O: 0.04 μ_B). As a consequence, this leads to a larger splitting in energy of the Pd-dominated surface states, as shown in *SI Appendix*, Fig. S4, but does not qualitatively influence any of the conclusions presented here.

ACKNOWLEDGMENTS. We thank C. Hooley, J. Jung, and J. Lee for useful discussions. We gratefully acknowledge support from the European Research Council (through the QUESTDO project, 714193), the Engineering and Physical Sciences Research Council, United Kingdom (Grant EP/I031014/1), the Royal Society, the Max-Planck Society, and the International Max-Planck Partnership for Measurement and Observation at the Quantum Limit. We thank Diamond Light Source for access to Beamline I05 (Proposals SI12469, SI14927, and SI16262), which contributed to the results presented here. V.S., L.B., and O.J.C. acknowledge the Engineering and Physical Sciences Research Council for PhD studentship support through Grants EP/L015110/1, EP/G03673X/1, and EP/K503162/1, respectively, and I.M. acknowledges studentship support from the International Max-Planck Research School for Chemistry and Physics of Quantum Materials.

1. Mannhart J, Schlom DJ (2010) Oxide interfaces – An opportunity for electronics. *Science* 327:1607–1611.
2. Zubko P, Gariglio S, Gabay M, Ghosez P, Triscone J-M (2011) Interface physics in complex oxide heterostructures. *Annu Rev Condens Matter Phys* 2:141–165.
3. Hwang H, et al. (2012) Emergent phenomena at oxide interfaces. *Nat Mater* 11:103–113.
4. Gozar A, et al. (2008) High-temperature interface superconductivity between metallic and insulating copper oxides. *Nature* 455:782–785.
5. Chakhalian J, et al. (2006) Magnetism at the interface between ferromagnetic and superconducting oxides. *Nat Phys* 2:244–248.
6. Reyren N, et al. (2007) Superconducting interfaces between insulating oxides. *Science* 317:1196–1199.
7. Boris A, et al. (2011) Dimensionality control of electronic phase transitions in nickel-oxide superlattices. *Science* 332:937–940.
8. Monkman EJ, et al. (2012) Quantum many-body interactions in digital oxide superlattices. *Nat Mater* 11:855–859.
9. King PDC, et al. (2014) Atomic-scale control of competing electronic phases in ultrathin $LaNiO_3$. *Nat Nanotechnol* 9:443–447.
10. Wang Z, et al. (2016) Tailoring the nature and strength of electron-phonon interactions in the $SrTiO_3$ (001) 2D electron liquid. *Nat Mater* 15:835–839.
11. Ohtomo A, Hwang HY (2004) A high-mobility electron gas at the $LaAlO_3/SrTiO_3$ heterointerface. *Nature* 427:423–426.
12. Caviglia AD, et al. (2008) Electric field control of the $LaAlO_3/SrTiO_3$ interface ground state. *Nature* 456:624–627.
13. Brinkman A, et al. (2016) Magnetic effects at the interface between non-magnetic oxides. *Nat Mater* 6:493–496.
14. Nakagawa N, et al. (2005) Why some interfaces cannot be sharp. *Nat Mater* 5:204–209.
15. Thiel S (2006) Tunable quasi-two-dimensional electron gases in oxide heterostructures. *Science* 313:1942–1945.
16. Bell C, et al. (2009) Dominant mobility modulation by the electric field effect at the $LaAlO_3/SrTiO_3$ interface. *Phys Rev Lett* 103:226802.
17. Siemons W, et al. (2007) Origin of charge density at $LaAlO_3$ on $SrTiO_3$ heterointerfaces: Possibility of intrinsic doping. *Phys Rev Lett* 98:216803.
18. Xie Y, Hikita Y, Bell C, Hwang HY (2011) Control of electronic conduction at an oxide heterointerface using surface polar adsorbates. *Nat Commun* 2:494.
19. Yu L, Zunger A (2014) A polarity-induced defect mechanism for conductivity and magnetism at polar–nonpolar oxide interfaces. *Nat Commun* 5:5118.
20. Reinle-Schmitt ML, et al. (2012) Tunable conductivity threshold at polar oxide interfaces. *Nat Commun* 12:2846–2851.
21. Bristowe NC, Littlewood PB, Artacho E (2011) Surface defects and conduction in polar oxide heterostructures. *Phys Rev B* 83:205405.
22. Gariglio S, Gabay M, Triscone J-M (2016) Research update: Conductivity and beyond at the $LaAlO_3/SrTiO_3$ interface. *APL Mater* 4:060701.
23. Shannon RD, Prewitt CT, Rogers DB (1971) Chemistry of noble metal oxides. II. Crystal structures of platinum cobalt dioxide, palladium cobalt dioxide, copper iron dioxide, and silver iron dioxide. *Inorg Chem* 10:719–723.
24. Shannon RD, Rogers DB, Prewitt CT (1971) Chemistry of noble metal oxides. I. Syntheses and properties of ABO_2 delafossite compounds. *Inorg Chem* 10:713–718.
25. Shannon RD, Rogers DB, Prewitt CT, Gillson JL (1971) Chemistry of noble metal oxides. III. Electrical transport properties and crystal chemistry of ABO_2 compounds with the delafossite structure. *Inorg Chem* 10:723–727.
26. Tanaka M, Hasegawa M, Takei H (1996) Growth and anisotropic physical properties of $PdCoO_2$ single crystals. *J Phys Soc J* 65:3973–3977.
27. Takatsu H, et al. (2007) Roles of high-frequency optical phonons in the physical properties of the conductive delafossite $PdCoO_2$. *J Phys Soc Jpn* 76:104701.
28. Mackenzie AP (2017) The properties of ultrapure delafossite metals. *Rep Prog Phys* 80:032501.
29. Cheong SW, Mostovoy M (2007) Multiferroics: A magnetic twist for ferroelectricity. *Nat Mater* 6:1476–1122.
30. Kawazoe H, et al. (1997) P-type electrical conduction in transparent thin films of $CuAlO_2$. *Nature* 389:939–942.
31. Singh DJ (2007) Electronic and thermoelectric properties of $CuCoO_2$ density functional calculations. *Phys Rev B* 76:085110.
32. Hicks CW, et al. (2012) Quantum oscillations and high carrier mobility in the delafossite $PdCoO_2$. *Phys Rev Lett* 109:116401.
33. Takatsu H, et al. (2013) Extremely large magnetoresistance in the nonmagnetic metal $PdCoO_2$. *Phys Rev Lett* 111:056601.
34. Kushwaha P, et al. (2015) Nearly free electrons in a 5d delafossite oxide metal. *Sci Adv* 1:e1500692.
35. Kim K, et al. (2009) Fermi surface and surface electronic structure of delafossite $PdCoO_2$. *Phys Rev B* 80:035116.
36. Noh HJ, et al. (2009) Anisotropic electric conductivity of delafossite $PdCoO_2$ studied by angle-resolved photoemission spectroscopy. *Phys Rev Lett* 102:256404.
37. Sunko V, et al. (2017) Maximal Rashba-like spin splitting via kinetic-energy-coupled inversion-symmetry breaking. *Nature* 549:492–496.
38. Bychkov YA, Rashba EI (1984) Properties of a 2D electron gas with lifted spectral degeneracy. *JETP Lett* 39:78–81.
39. Noh HJ, et al. (2009) Orbital character of the conduction band of delafossite $PdCoO_2$ studied by polarization-dependent soft x-ray absorption spectroscopy. *Phys Rev B* 80:073104.
40. Chikina A, et al. (2014) Strong ferromagnetism at the surface of an antiferromagnet caused by buried magnetic moments. *Nat Commun* 5:3171.
41. Takatsu H, et al. (2009) Critical behavior of the metallic triangular-lattice Heisenberg antiferromagnet $PdCrO_2$. *Annu Rev Mater Res* 79:104424.
42. Sobota JA, et al. (2013) Electronic structure of the metallic antiferromagnet $PdCrO_2$ measured by angle-resolved photoemission spectroscopy. *Phys Rev B* 88:125109.
43. Huang B, et al. (2017) Layer-dependent ferromagnetism in a van der Waals crystal down to the monolayer limit. *Nature* 546:270–273.
44. Gong C, et al. (2017) Discovery of intrinsic ferromagnetism in 2D van der Waals crystals. *Nature* 546:265–269.
45. Banerjee S, Erten O, Randeria M (2013) Ferromagnetic exchange, spin–orbit coupling and spiral magnetism at the $LaAlO_3/SrTiO_3$ interface. *Nat Phys* 9:626–630.
46. Bhattacharya A, May SJ (2014) Magnetic oxide heterostructures. *Phys Rev B* 44:65–90.
47. Fukami S, et al (2016) Magnetization switching by spin-orbit torque in an antiferromagnet–ferromagnet bilayer system. *Nat Mater* 15:535–541.
48. Takatsu H, et al. (2010) Single crystal growth of the metallic triangular-lattice antiferromagnet $PdCrO_2$. *J Cryst Growth* 312:3461–3465.
49. Hoesch M, et al. (2017) A facility for the analysis of the electronic structures of solids and their surfaces by synchrotron radiation photoelectron spectroscopy. *Rev Sci Inst* 88:013106.
50. Koepernik K, et al. (1999) Full-potential nonorthogonal local-orbital minimum-basis band-structure scheme. *Phys Rev B* 59:1743–1757.
51. Opahle I, et al. (1999) Full-potential band-structure calculation of iron pyrite. *Phys Rev B* 60:14035–14041.
52. Perdew JP, et al. (1996) Generalized gradient approximation made simple. *Phys Rev Lett* 77:3865–3868.